Clustering of [C IV]-selected AGN and galaxies at z=1.5-3 in the zCOSMOS Deep survey

J. T. Johnson,[1] N. Cappelluti,[1, 2, 3, 4] M. C. Powell,[2, 5] R. Gillii,[4] M. Mignoli,[4] and M. M. Lozio[4]

[1]Physics Department, University of Miami, Coral Gables, FL 33155, USA
[2]Yale Center for Astronomy and Astrophysics, and Physics Department, Yale University, PO Box 2018120, New Haven, CT 06520-8120
[3]YCAA
[4]OABO
[5]Stanford

ABSTRACT

We investigate the clustering of CIV selected AGN and galaxies in the zCOSMOS Deep survey, and compare the results with X-ray selected AGN from the same survey area. By comparing the clustering analysis of the two selection methods, we investigate whether or not the AGN samples reside in similar environments. For CIV selected AGN, we find a bias of $3.69^{+0.99}_{-1.37}$ which corresponds to an average log dark matter halo mass of $12.65^{+0.31}_{-0.73}$. Similarly, for X-ray selected AGN, we find a bias of $3.40^{+0.78}_{-1.03}$ which corresponds to an average log dark matter halo mass of $12.57^{+0.28}_{-0.57}$. These results are consistent with the stellar mass estimates of the host galaxies of each sample via the expected stellar-mass-halo-mass relation. This suggests that CIV and X-ray -selected AGN are hosted in similar environments, with no significant selection biases between them.

Keywords: AGN

1. INTRODUCTION

The link between structure growth, galaxy evolution and active galactic nuclei (AGN) is one of the most intriguing as speculated topic in modern astrophysics. On top of that, the study of how galaxies populate the Large Scale Structures (LSS) of the universe is a fundamental test for Cosmology. The study of galaxy clustering at low redshift has been employed as precise probes of cosmological parameters and the assembly of LSS along cosmic history (Peacock et al. 2001; Guzzo et al. 2008). However, the measure of clustering of galaxies is strongly dependent on the physical parameters of the selected galaxy (cit.). Different galaxy classes may or may not exist in the same environments and therefore are capable of tracing the structures where they most likely live. Recent works show that, both at z<1 (Marulli et al. 2013) and at 2<z<5 (Durkalec et al. 2015) galaxy clustering is strongly dependent on the stellar mass and/or on their luminosity. In the redshift range 1.5<z<3, where the cosmic star formation peaks, galaxy clustering in real space has been poorly studied due to the difficulty of collect large samples of spectroscopic redshifts . In that

Corresponding author: N. Cappelluti
ncappelluti@miami.edu

redshift range galaxies convert very efficiently gas into stars and, at the same time, we witness the cosmic peak of AGN activity (cit.). It has been shown that AGN preferentially reside in group sized overdensities ?Powell et al. (see e.g. 2018); ?); ?); ?. Powell et al. (2018); ? showed that at low redshift that AGN clustering is mostly driven by the total stellar mass of the host galaxy with a clustering amplitude scaling with the mass of the host.

In this framework it is important to understand the level of biasing of any given galaxy class to understand if and how the environments shape their evolution.

While there is a growing evidence of the relation between star formation episodes and Active Galactic Nuclei (AGN) activity (refs.), we are still far from having a clear picture of the relation between AGN activity, star formation and the Dark Matter Halos (DMHs) hosts of galaxies.

The picture is then complicated by the different criteria used in the literature to select AGN samples to derive their clustering and environmental properties.

Since AGN are expected to play a fundamental role in galaxy evolution and on star formation it is important to study AGN and galaxy clustering using the same sample to avoid selection biases that are common when comparing different galaxy populations.
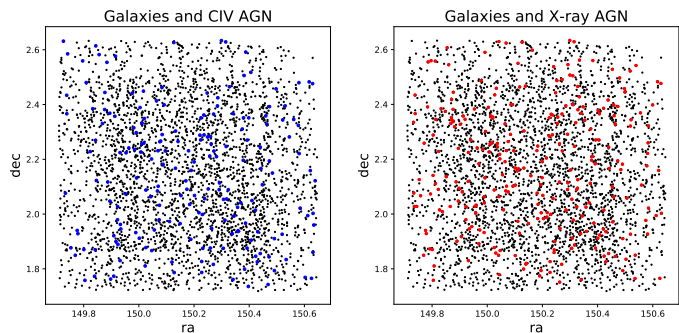
Figure 1. The sky distribution of the CIV AGN (blue), Xray AGN (red) and galaxies (black)

Multi-wavelength data facilitates studies of AGN since obscuration by gas and dust biases selection in any given band (Hickox & Alexander 2018). However, selection of luminous X-ray sources results in the most complete sample.

In this paper we take advantage of the unique capabilities of the zCOSMOS-deep survey to select galaxies and AGN at redshift 1.5<z<3.5 in a self consistent way and determine the influence of stellar mass on the clustering parameter on both galaxy and AGN populations. In addition, we also compare our results to X-ray selected AGN from the Chandra COSMOS-legacy survey within the same sky area for reference and comparison between selection methods.

Throughout this paper we assume the Planck 2015 (ref) cosmological model ($H_0 = 100h$ km/s/Mpc, $h = 0.677$, $\Omega_{m,0} = 0.307$, $\Omega_{b,0} = 0.0486$).

2. SAMPLE SELECTION

COSMOS is a xx deg^2 field with extensive, deep multiwavelength coverage. With data ranging from X-ray to radio wavelengths, it is ideal for measuring the evolution of galaxies and AGN on a cosmic scale.

2.1. *Galaxy Sample*

The zCOSMOS survey (Lilly et al. 2007) collected ∼28000 galaxy redshifts in the inner 1 deg^2 of the COSMOS field (Scoville 2007) using the VIMOS spectrograph on the Very Large Telescope (VLT). The survey was performed in two stages: the zCOSMOS-bright which collected ∼20000 spectra down to magnitude limit $i < 22.5$ and the zCOSMOS-deep which has been designed to select faint 1.4< z <3.5 galaxies.

Since it was intentionally designed to select high-z galaxies, the zCOSMOS-deep sample was selected via BzK color selection, with a K$_{AB}$ cut at 23.5, complemented with ugr selection. In order to provide targets suitable for optical spectroscopy with VIMOS, an additional blue magnitude (B$_{AB}$ < 25.25) selection was

adopted. A detailed description of the selection criteria is carefully reported in (Diener et al. 2013). In this work we'll use zCOSMOS-deep as a starting sample for our analysis. In the left panel of Figure 3 we show the redshift distribution of the overall sample.

For the purpose of this paper we used galaxies with spectro-z quality 2.5≥FLAG≤4.5, 9.3≥FLAG≤9.5 and 22.5≤FLAG≥24.5. Among these we restricted our selection to galaxies with $1.4 < z < 3.5$. As a result our final sample of galaxies contains 2587 sources.

An important parameter that we used for our clustering analysis is the stellar mass of the galaxies of this sample. Using a SED fitting technique we performed (which SED fitting code? Wavelength span and assumptions?), we were to able to accurately estimate their stellar masses. Typical stellar mass uncertainties?? Discussing details of mass estimates is beyond the scope of this paper but is broadly discussed in Bolzonella et al. (2000) and presented elsewhere for this sample elsewhere in this paper? Or another? Need reference/section specification. The distribution of the stellar masses in our sample is shown in the left panel of Figure 2. Figure references out-of-order

2.2. *CIV AGN Sample*

The C IV AGN sample analyzed in this paper was extracted from the parent zCOSMOS deep (ref.) sample by Mignoli et al. (in prep.), using the high ionization C IV λ1540 Å emission line as a proxy for the nuclear activity. The C IV line is the more common spectral feature in the zCOSMOS-Deep spectra, being included in the observed spectral range for the wide redshift interval $1.5 < z < 3$. In this redshift range, more than 2800 VIMOS spectra with good-to-high quality redshifts were analyzed, providing 192 zCOSMOS-Deep objects with a clearly detected (EW>5Å) C IV emission line. Since the spectral resolution of VIMOS zCOSMOS-Deep spectra is moderate (instrumental FWHM ≈ 1350 km/s), we used 2000 km/s as threshold values between Type I and Type II AGN. While unobscured (Type I) AGN are easily identifiable due to their broad line profile, the obscured (Type II) AGN classification could be more ambiguous because of the possible degeneration of narrow AGN emission lines with star formation lines. Although the presence of significant C IV emission is a powerful indicator of a high ionization potential and therefore AGN activity, Mignoli et. al also demonstrates that the C IV-selected Type II AGN occupy a well defined locus in the UV lines ratio diagram (e.g. Nagao et al. 2006), consistent with photoionization model from an active nucleus. Based on the above criterion we selected two bonafide samples of 102 Type I AGN and 92 Type II
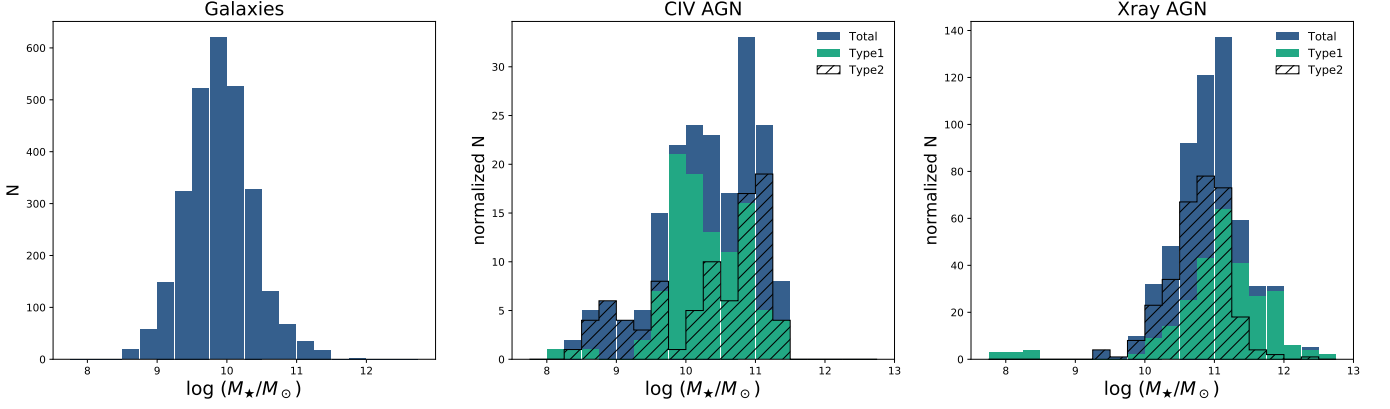
Figure 2. The stellar mass distribution of the Galaxy sample as well as the AGN samples selected by CIV and Xray emmision used for clustering analysis. The AGN samples are also split into Type I and Type II AGN.
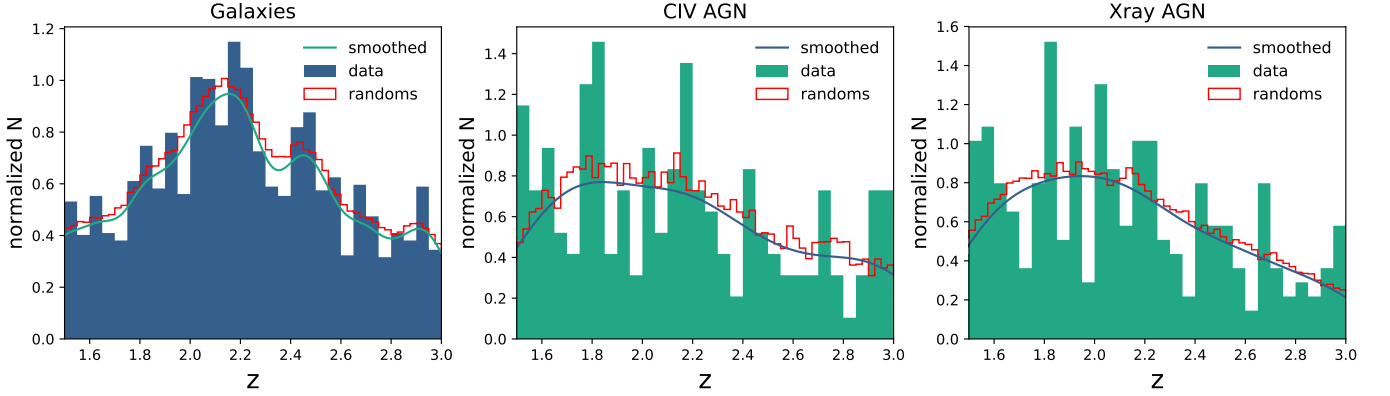

Figure 3. Left, in *blue*, the redshift distribution of tracers galaxies, the *green continuous line* represents the smoothed redshift distribution of galaxies used to create random samples, the *red line* is the galaxy random sample redshift distribution. Center, in *green*, the redshift distribution of CIV selected AGN, the *blue continuous line* represents the smoothed redshift distribution of AGN used to create random samples, the *red line* is the AGN random sample redshift distribution. Right, in *green*, the redshift distribution of Xray selected AGN, the *blue continuous line* represents the smoothed redshift distribution of AGN used to create random samples, the *red line* is the AGN random sample redshift distribution.

AGN. Their redshift distributions are show in the center panel of Figure 3. How many Type II only satisfied one criterion?

Thanks to the large amount of photometric data in the COSMOS field, we were able to estimate the stellar masses of the host galaxies of the 194 C IV AGN by following the the prescription of Bongiorno et al. (2012). We performed a broad band fit of the NIR/Optical SED with a large number of host galaxy plus AGN templates as models. We refer the reader to Bongiorno et al. (2012) for a detailed description of the procedure. The results of this fit are summarized in a histogram in the right panel of Figure 3. The mean host stellar mass of the AGN sample is Log($M_\star$)∼10.3 with a median of Log($M_\star$)∼10.4. Typical uncertainties?? Interestingly the distribution seems bimodal with the two main peaks at Log($M_\star$)∼10.0 and Log($M_\star$)∼11.0 with Type I AGN slightly more massive than Type II AGN. We compared

the masses obtained for AGN with the method of (Bolzonella et al. 2000) and with that of Bongiorno et al. (2012) and found a good agreement for Type II AGN where the host galaxy is the dominant component to the total emission. Such an agreement disappears for Type I AGN where the nuclear components are by far stronger than the the host galaxy.

2.3. X-ray AGN sample

The Chandra COSMOS legacy survey has a contiguous area of 2.2 deg^2 containing 4016 X-ray point sources identified by 4.6 Ms Chandra space telescope time (Civano et al. 2016). Sources with $det_{ml} > 10.8$ are considered X-ray detections. 3619 of these sources have optical and IR counterparts, as described in Marchesi et al. (2016).

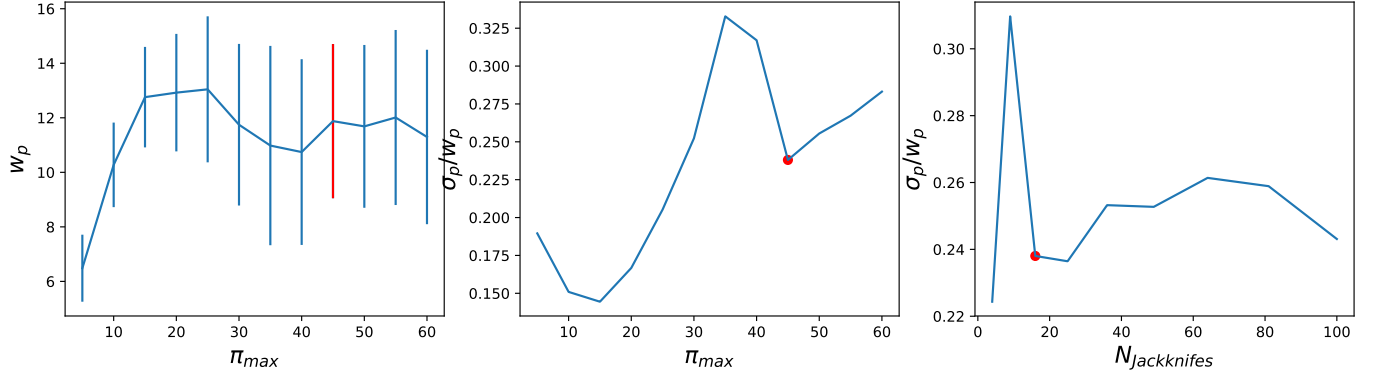From these AGN, we select those within the same sky area as the C IV sample with 149.710846 < ra <

Figure 4. Results of π_{max} and Jackknife (M) tests for the C IV AGN sample. The selected vales of $\pi_{max} = 45$ and $M = 16$ are shown in red.

150.645706 and $1.718882 < dec < 2.63344$. We further restrict the sample to lie within the same redshift range as the C IV AGN: $1.475 < z < 3.05$. The sky distribution of the X-ray AGN sample is shown in red in Figure 1. Our resulting X-ray sample contains 552 AGN.

3. METHODOLOGY

3.1. *Two point statistics*

The two-point autocorrelation function (ACF, $\xi(r)$) is a measure that evaluates the excess probability over random of finding a pair with an object in the volume dV_1 and another in the volume dV_2, separated by a comoving distance r so that $dP=n[1+\xi(r)]dV_1dV_2$, where n is the mean space density of the object subject of the investigation. A sample with a completely random distribution will have $\xi = 0$, while a clustered sample will have an increased amplitude of ξ.

We compute the ACF in spatial bins perpendicular (r_p) and parallel (π) to the line of sight, estimated by following Fisher et al. (1994), if v_1 and v_2 are the redshifts of galaxy 1 and 2, $\mathbf{s}=\mathbf{v}_1\text{-}\mathbf{v}_2$ is the redshift space separation and $\mathbf{l}=1/2\mathbf{v}_1+\mathbf{v}_2$ is the observer's line of sight. r_p and π are the comoving separations perpendicular and along the line of sight and are defined as:

$$\pi = \frac{\mathbf{s} \cdot \mathbf{l}}{|\mathbf{l}|}, \qquad (1)$$

$$r_p^2 = \mathbf{s} \cdot \mathbf{s} - \pi^2. \qquad (2)$$

The ACF has been estimated by using the minimum variance estimator described by Landy & Szalay (1993):

$$\xi(r_p, \pi) = \frac{DD - 2DR + RR}{RR} \qquad (3)$$

where DD, DR, and RR are the normalized number of data-data, data-random, and random-random source pairs, respectively falling within the r_p and π bins. We

use the `CorrFunc` software for pair counting (Sinha & Garrison 2017).

Measuring the two point correlation function in redshift surveys requires the consideration that redshift measurements are a combination of peculiar velocities and the Hubble flow. This degeneracy may cause a biased estimate of the distance. To avoid the effect of redshift space distortions, we computed the projected ACF (Davis & Peebles 1983b). This is defined as:

$$w(r_p) = 2 \int_0^{\pi_{max}} \xi(r_p, \pi)d\pi \qquad (4)$$

The integration limit π_{max} is critical in estimating the amplitude of $w_p(r_p)$. A choice π_{max} too small would produce an underestimate of $w_p(r_p)$, while large values of π_{max} would introduce noise in the ACF and increase computational time. The optimal value was chosen by computing w_p, averaged over scales from $1-10$ Mpc h^{-1}, for π_{max} varying from 5 to 60 Mpc h^{-1}. We tested the convergence of the integral as function of the scale for each of the data samples, and choose π_{max} such that the 2-halo term of w_p converges and higher values would only introduce noise to the ACF.

The results of the π_{max} tests for C IV AGN are shown in Figure 4. The first panel shows the convergence of the sample at π_{max}=20, and the second panel shows that increasing π_{max} past this value introduces noise. The galaxies display a similar convergence, however the Xray AGN do not converge until π_{max}=45. Therefore, in order to maintain consistency, we choose π_{max}=45. While this choice, shown in red in Figure 4, may introduce some noise into the C IV and galaxy samples, it guarantees that all samples will converge and allows for consistency.

The C IV AGN sample is too small to estimate $w_p(r_p)$ directly. The sample of galaxies covers, with a large enough number of sources, the same redshift interval of 1.5 to 3; consequently, we derived $w_p(r_p)$ of AGN from
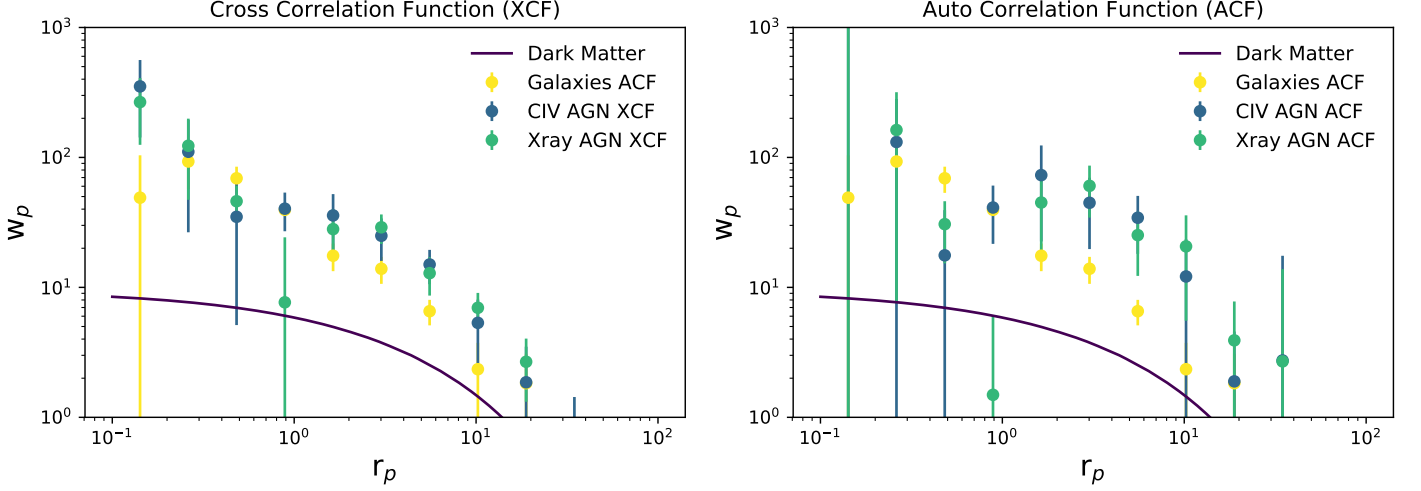
Figure 5. The projected cross correlation function (XCF) and computed projected auto correlation function (ACF) of the AGN and galaxies. CIV selected AGN XCF are shown in blue, X-ray selected AGN XCF are shown in green, and the galaxy sample ACF is shown in yellow. For comparison, $w_{p,DM}$ at $z =$?? is shown in purple.

the AGN-galaxy cross-correlation function, along with the ACF of galaxies, in order to improve statistics. The cross-correlation function (XCF) is computed similarly to the ACF, using the Landy-Szalay estimator (Landy & Szalay 1993):

$$\xi(r_p, \pi) = \frac{D_1 D_2 - D_1 R_2 - R_1 D_2 + R_1 R_2}{R_1 R_2} \quad (5)$$

where DD, DR, and RR are data-data, data-random, and random-random pairs respectively, corresponding to the sample indicated by their subscripts. For AGN-galaxy cross-correlation, the subscripts 1 and 2 would indicate AGN and galaxy samples. In the case of the ACF, the subscripts refer to the same sample thus the formula reduces to Equation 3.

The autocorrelation of the AGN samples ($w_{p,AA}$) were then computed via the estimation method found in Coil et al. (2009) and more recently used in Mendez et al. (2016):

$$w_{p,AA} = \frac{(w_{p,AG})^2}{w_{p,GG}} \quad (6)$$

where $w_{p,AG}$ is the AGN-galaxy cross-correlation , and $w_{p,GG}$ is the autocorrelation of galaxies. The auto-correlation function for both AGN samples are shown in comparison to galaxy ACF in the right panel of Figure 5. This estimate is valid for the 2-halo term of $w_p(r_p)$, i.e., the amplitude on 1-10 Mpc h^{-1}scales that measures clustering of galaxies and AGN in distinct dark matter halos. The 2-halo term is used for halo mass estimation.

3.2. Error Estimation

To estimate uncertainties of the correlation function, we utilized the jackknife re-sampling technique. This technique involves splitting each sample into various patches of sky, and repeating the correlation function measurement when excluding each patch (w_k). The resulting changes in w_p are captured in the covariance matrix (C) defined by:

$$C_{i,j} = \frac{M}{M-1} \sum_{k}^{M} \Big[w_{p,k}(r_{p,i}) - \langle w_p(r_{p,i}) \rangle \Big] \\ \times \Big[w_{p,k}(r_{p,j}) - \langle w_p(r_{p,j}) \rangle \Big] \quad (7)$$

The covariance matrix defines the w_p errors for each bin of r_p as $\sigma_i = \sqrt{C_{i,i}}$.

The number of jackknife patches (M) is important because few patches will provide inaccurate estimations by excluding large chunks of data; however, a large number of jackknife samples drastically increase computational time with little gain in error estimation. After conducting a test varying M, shown in the third panel of Figure 4, we found error estimates to be consistent for $M >= 16$. Thus, to minimize computational time, we use $M = 16$. Each resulting patch contains $2 - 10\%$ of the data.

3.3. random catalog generation

This section should go before the Error Estimation section

An accurate estimate of the distribution function of the random samples is crucial to obtain a reliable estimate of $\xi(r_p, \pi)$. Several observational biases must be taken into account when generating a random sample of objects in a flux limited survey. In particular, in order to reproduce the selection function of the survey, one has to carefully reproduce the space and flux
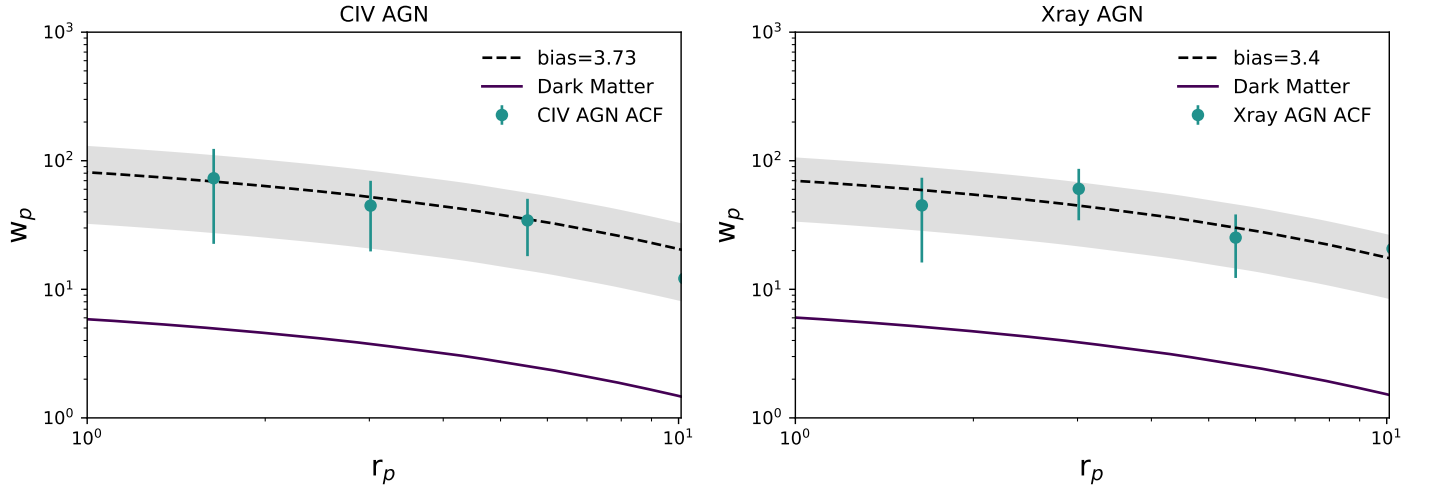
Figure 6. The projected auto correlation function of CIV and Xray selected AGN, zoomed in on the 2-halo term on scales of 1-10 Mpc h^{-1}. The dashed black lines correspond to the bias relative to $w_{p,DM}$ (purple), and the grey shaded region corresponds to the one-σ errors for the bias.

distributions of the sources, since the sensitivity of the survey in not homogeneous on the sky. Producing can be extremely time consuming especially in the case of a spectroscopically selected sample where the selection function is very complicated. To circumvent this obstacle we decided to adapt the technique described by Gilli et al. (2009). Simulated random galaxies and AGN were placed at their sky position in the optical catalog, and then distributed randomly in space according to their smoothed redshift distribution obtained with a Gaussian kernel with σ_z=0.2 for both galaxies and AGN. The random and real redshift distribution used for the whole sample of galaxies are shown in Figure 3.

3.4. Halo Model analysis

The projected ACF signal can be divided into two main components, one produced by pairs of sources within the same halo (one-halo term, 1h) and one produced by source pairs belonging to separate distinct halos (2-halo term, 2h) (Cooray & Sheth 2002). The superposition of the 1h and 2h terms yields the galaxy correlation function:

$$w_p(r_p) = w_{p,1h}(r_p) + w_{p,2h}(r_p) \qquad (8)$$

While the 1h-term dominates at scales $\lesssim 1$ Mpc h^{-1}, the contribution of the 1h-term is negligible at scales > 1 Mpc h^{-1}. Therefore we will consider that all the power produced at such scales is solely due to the 2h-term. The amplitude of the 2h-term provides a pathway to estimate the average host halo mass that the sample resides in (Tinker et al. 2010).

We follow the process for halo mass estimation outlined in Powell et al. 2020, which we have detailed below.

The respective amplitudes between the 2h-term and that of dark matter halos, averaged over scales of 1-10 Mpc h^{-1}, defines an AGN bias ratio:

$$b_{AGN} = \sqrt{\frac{w_{p,AGN}}{w_{p,DM}}} \quad . \qquad (9)$$

$w_{p,DM}$ is the projected dark matter correlation function, defined similarly to the projected correlation function of galaxies (Eq. 4) by the integration of the real space correlation function through redshift space (Davis & Peebles 1983a):

$$w_{p,DM}(r_p) = 2 \int_{r_p}^{r_{\max}} \frac{\xi_{DM}(r) r \, dr}{\sqrt{r^2 - r_p^2}} \quad , \qquad (10)$$

where $r_{\max} = \sqrt{\pi_{\max}^2 + r_p^2}$ and ξ_{DM} is the Fourier transform of $P(k)$:

$$\xi_{DM}(r) = \frac{1}{2\pi^2} \int_{r_p}^{\infty} P(k) k^2 \left(\frac{\sin(kr)}{kr} \right) dk \quad . \qquad (11)$$

$P(k)$, the linear power spectrum, is calculated with the transfer function from Eisenstein & Hu (1998), using a spectral index $n = 1$. We calculate $P(k)$ using `hmf`, a publicly available software (Murray 2014).

The typical host halo mass of the AGN was inferred from the bias and effective redshift of the sample, by comparing to the Tinker et al. (2010) halo bias relation, $b(\nu)$. $\nu = \delta_c/\sigma(M_h)$, where δ_c is the critical overdensity for collapse (1.686; reference) and $\sigma(M_h)$ is the rms density fluctuations within a sphere of mass M:

$$\sigma^2(M) = \int P(k,z) \hat{W}(k,R) k^2 dk \qquad (12)$$

catalog	type	bias	redshift	log M_h [M$_\odot$]
CIV	Total	$3.69^{+0.99}_{-1.37}$	2.16	$12.65^{+0.31}_{-0.73}$
	I	$2.94^{+0.95}_{-1.47}$	2.15	$12.33^{+0.41}_{-1.36}$
	II	$4.83^{+1.57}_{-2.44}$	2.20	$12.98^{+0.33}_{-1.03}$
Xray	Total	$3.40^{+0.78}_{-1.03}$	2.12	$12.57^{+0.28}_{-0.57}$
	I	$3.38^{+0.78}_{-1.03}$	2.12	$12.56^{+0.29}_{-0.58}$
	II	$3.37^{+0.78}_{-1.03}$	2.12	$12.56^{+0.29}_{-0.58}$
Galaxies		$1.90^{+0.21}_{-0.24}$	2.24	$11.46^{+0.21}_{-0.30}$

Table 1. Bias and halo mass measurements of CIV and X-ray-selected quasars, split into spectral types. Values for the galaxy sample are also shown for comparison.

$\hat{W}(k, R)$ refers to a top-hat window function, and $R = (3M_h/4\pi\bar{\rho})^{1/3}$ where $\bar{\rho}$ is mean density of the universe. The AGN host halo mass is obtained via solving for M when setting the halo bias relation to the AGN bias: $b_{AGN} = b(z, M_h)$. z is the effective redshift of the sample:

where z is effective redshift (z_{eff}) of the sample, defined by:

$$z_{eff} = \frac{\Sigma_{i,j}(z_i + z_j)}{2N} \quad (13)$$

where i and j sum over all AGN pairs, and N is the total number of pairs.

4. RESULTS

4.1. Clustering of CIV vs X-ray selected AGN

We performed the clustering analysis outlined above for both the CIV and X-ray AGN. Furthermore, we partitioned each sample into its spectral type classes to allow for comparison of Type I, Type II, and all AGN for each selection method. How are Type I/II X-ray AGN defined? The primary results are listed in Table 1 with the bias, redshift, and estimated dark matter halo mass for each AGN sample, as well as the galaxies for comparison.

Explicitly, we find that CIV AGN have a bias of $3.69^{+0.99}_{-1.37}$, corresponding to host halos of log mass $12.65^{+0.31}_{-0.73}$ [$M_\odot/h$]. This is comparable to the X-ray AGN which have a bias of $3.40^{+0.78}_{-1.03}$ and thus an average log halo mass of $12.57^{+0.28}_{-0.57}$ [$M_\odot/h$]. As a result, it is likely that these two samples reside within similar large-scale environments.

Our CIV and X-ray AGN are at effective redshifts of 2.16 and 2.12 respectively. Thus, a direct comparison of the bias measurement for CIV and X-ray AGN (shown in Figure 6, and Table 1) shows that the two selection criteria likely select AGN from similar environments. However, to more accurately compare the two
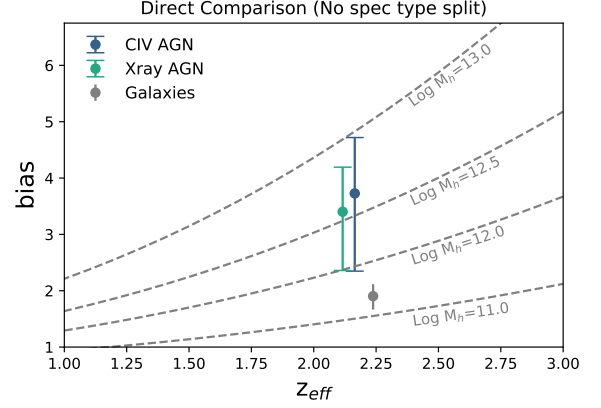

Figure 7. computed bias vs effective redshift. Points are shown CIV and Xray AGN. Grey dashed lines show curves for example halo masses.
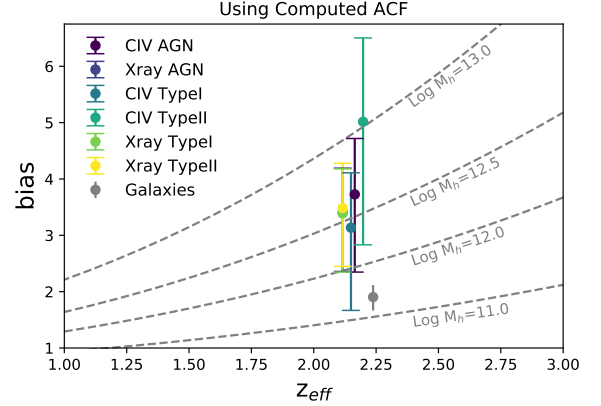

Figure 8. computed bias vs effective redshift. Points are shown CIV and Xray AGN as well as their Type I and Type II subsamples. Grey dashed lines show curves for example halo masses.

samples, we must take into account the effect of redshift on halo mass.

Figure 7 displays the bias versus the effective redshift of the samples. The grey dashed lines are references for various examples of dark matter halo masses. Here, we can more clearly see the similarity in halo mass resulting from the distinct AGN selection criteria. The proximity of the two samples suggests that both CIV and X-ray selected AGN reside in similar halo mass environments.

We also look at the effect of AGN spectral type on the average host halo mass. The values for Type I and Type II AGN are listed in Table 1 and displayed in Figure 8, which is identical to Figure 7 with the addition of the clustering results for the spectral type splits.

Here, the Type I, Type II, and total samples for X-ray AGN are consistent in terms of bias, effective redshift, and average halo mass. This is to be expected in the pic-

ture where Type I and II are the same objects viewed at different orientations angles (e.g., Urry& Padovani). C IV AGN, however have drastically different biases and therefore halo masses (although they are still within error of each other).

The distinction between Type I and Type II in the C IV could be a result of several factors. The C IV AGN had a bimodal split in the stellar mass distribution. When the log $M_\star$ distribution was split into Type I and Type II AGN, it becomes apparent that the two distinct peaks are from the two spectral types. Host galaxy stellar mass can influence the results of clustering analysis (see section 4.2); consequently, the different stellar mass distributions for Type I and Type II C IV AGN would create the observed distinction in expected halo mass by spectral type.

However, it could also be due to low number statistics. There are 192 AGN in the total sample, and merely 99 identified as Type I and 88 as Type II. Because there are so few sources, this could skew the results when the sample is split by spectral type.

4.2. *Galaxy clustering as a function of $M_\star$*

A notable result of previous investigations in several redshift ranges is the dependency of the clustering amplitude on the stellar mass of the galaxy sample (e.g. Viitanen et al. 2019, z∼1). Considering our sample size we were able to compute the ACF of our 2896 galaxies in three $M_\star$ bins of approximately equal size. The three bins have the following mass range: for low mass sample $Log(M_\star)$=8.4-9.6, for the medium mass sample $Log(M_\star)$=9.6-10.1and for the high mass sample $Log(M_\star)$=10.1-11.9. The properties of the sample are summarized in table ?? and we labeled the samples LMF, MMF and HMF, respectively. We also split each subsample in two redshift bins namely 1.4< z <2.2 and 2.0< z <3.0

5. DISCUSSIONS

6. CONCLUSIONS

7. ACKNOWLEDGMENTS

REFERENCES

Bolzonella, M., Miralles, J. M., & Pelló, R. 2000, A&A, 363, 476

Bongiorno, A., Merloni, A., Brusa, M., et al. 2012, MNRAS, 427, 3103

Civano, F., Marchesi, S., Comastri, A., et al. 2016, ApJ, 819, 62

Coil, A. L., Georgakakis, A., Newman, J. A., et al. 2009, ApJ, 701, 1484

Cooray, A., & Sheth, R. 2002, PhR, 372, 1

Davis, M., & Peebles, P. J. E. 1983a, ApJ, 267, 465

—. 1983b, ApJ, 267, 465

Diener, C., Lilly, S. J., Knobel, C., et al. 2013, ApJ, 765, 109

Durkalec, A., Le Fèvre, O., Pollo, A., et al. 2015, A&A, 583, A128

Eisenstein, D. J., & Hu, W. 1998, ApJ, 496, 605

Fisher, K. B., Davis, M., Strauss, M. A., Yahil, A., & Huchra, J. P. 1994, MNRAS, 267, 927

Gilli, R., Zamorani, G., Miyaji, T., et al. 2009, A&A, 494, 33

Guzzo, L., Pierleoni, M., Meneux, B., et al. 2008, Nature, 451, 541

Hickox, R. C., & Alexander, D. M. 2018, ARA&A, 56, 625

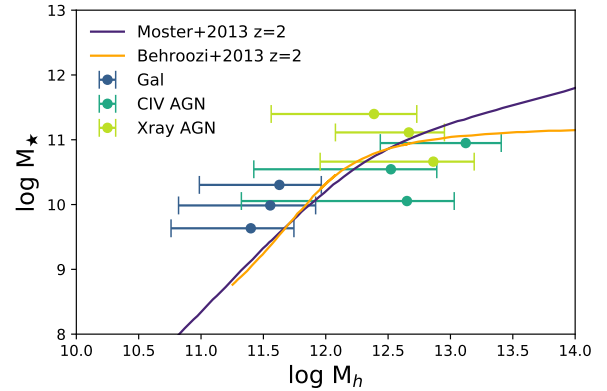Landy, S. D., & Szalay, A. S. 1993, ApJ, 412, 64

Figure 9. Stellar mass as a function of halo mass. Models from literature shown in comparison

Lilly, S. J., Le Fèvre, O., Renzini, A., et al. 2007, ApJS, 172, 70

Marchesi, S., Civano, F., Elvis, M., et al. 2016, ApJ, 817, 34

Marulli, F., Bolzonella, M., Branchini, E., et al. 2013, A&A, 557, A17

Mendez, A. J., Coil, A. L., Aird, J., et al. 2016, ApJ, 821, 55

Murray, S. 2014, HMF: Halo Mass Function calculator, Astrophysics Source Code Library, ascl:1412.006

Nagao, T., Maiolino, R., & Marconi, A. 2006, A&A, 459, 85
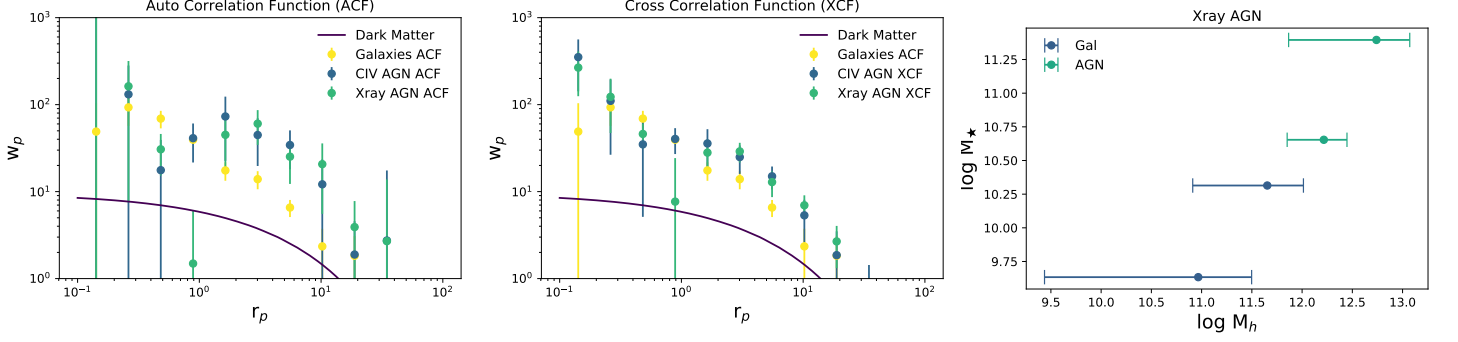
Figure 10. From left to right ACF of low, medium and high mass galaxy at $< z >$2.1, respectively.

Figure 11. The cross correlation function of the CIV selected Type I AGN with galaxies at 1.4<z<3.5 (*red open circles*). Compared the galaxy autocorrelation function (*blue filled circles*) and the CIV selected AGN autocorrelation function (*green triangles*)

Figure 13. The bias of galaxies (filled circles) and AGNs (filled triangles) at z~2.1 as a function of the stellar mass computed by MB. For AGN we use the stellar mass computed by AB
.

Peacock, J. A., Cole, S., Norberg, P., et al. 2001, Nature, 410, 169

Powell, M. C., Cappelluti, N., Urry, C. M., et al. 2018, ApJ, 858, 110

Scoville, N. 2007, in Astronomical Society of the Pacific Conference Series, Vol. 375, From Z-Machines to ALMA: (Sub)Millimeter Spectroscopy of Galaxies, ed. A. J. Baker, J. Glenn, A. I. Harris, J. G. Mangum, & M. S. Yun, 166

Sinha, M., & Garrison, L. 2017, Corrfunc: Blazing fast correlation functions on the CPU, Astrophysics Source Code Library, ascl:1703.003

Tinker, J. L., Robertson, B. E., Kravtsov, A. V., et al. 2010, ApJ, 724, 878

Viitanen, A., Allevato, V., Finoguenov, A., et al. 2019, A&A, 629, A14

Figure 12. The cross correlation function of the CIV selected Type II AGN with galaxies at 1.4<z<3.5 (*red open circles*). Compared the galaxy autocorrelation function (*blue filled circles*) and the CIV selected AGN autocorrelation function (*green triangles*)